

Electronic Supplementary Information

A one-step deep eutectic solvents assisted synthesis of carbon nitride/metal oxide composites for photocatalytic nitrogen fixation

Hongyu Mou^{[a]#}, Jinfang Wang^{[a]#}, Deliang Zhang,^{[b]#} Dongkun Yu,^[a]
Wenjun Chen,^[a] Debao Wang,^{*[b]} and Tiancheng Mu^{*[a]}

[a] Department of Chemistry, Renmin University of China, No 59 Zhongguancun Street, Beijing 100872, China. E-mail: tcmu@ruc.edu.cn

[b] Shandong Key Laboratory of Biochemical Analysis, College of Chemistry and Molecular Engineering, Qingdao University of Science and Technology, Qingdao 266042, China. E-mail: dbwang@qust.edu.cn

These authors contributed equally to this work.

Table of the contents

1. Experiment Section
2. Supplementary Figures and Discussion
3. Supplementary Tables
4. References

1. Experiment Section

Photocatalytic Activity Test.

All photocatalytic activity experiments were conducted at ambient temperature using a 300 W xenon lamp. For the fixation of molecular nitrogen, 0.1 g of photocatalyst was added into 100 mL of distilled water in a reactor. The reactor was equipped with water circulation in the outer jacket in order to maintain at room temperature of 25 °C. The catalyst mixture is uniformly dispersed by ultrasound. Three milliliters of the solution was taken out each 30 min and after centrifuged to remove the photocatalyst, and the concentration was monitored by colorimetry with the PerkinElmer Lambda750 UV-vis spectrometer. Xenon light (PLS-SXE300D/DUV, PerfectLight Co. Ltd. China) with total light intensity of 200 mW/cm² was utilized as light source. Oxidation of water was carried out in a reaction cell under 300 W xenon lamp. At certain time intervals, liquid (NH₃) was determined by the Nessler's reagent.

Photoelectrochemical measurements.

All the electrochemical and photoelectrochemical (PEC) measurements were carried out on a Princeton Applied Research Modulelab using a three-electrode system with a Pt sheet as the counter electrode, saturated calomel electrode (Ag/AgCl) as the reference electrode, and the as-prepared photoanodes as the working electrode. The Mott-Schottky (MS) plots were measured in a 0.5 M KPi buffer (pH 7) at a frequency of 800 Hz and amplitude of 10 mV under the dark condition. Electrochemical impedance spectroscopy (EIS) was carried out in the frequency range of 0.5 Hz-10⁵ Hz, with AC voltage amplitude of 10 mV in a 0.5 M Na₂SO₄ aqueous solution. For photocurrent density vs. potential (J-V) and photocurrent density vs. time (J-t) curves, the working electrode with an area of 1×1 cm² was immersed in 0.5 M Na₂SO₄ aqueous solution and illuminated using a 300 W Xe-lamp with a light density of 200 mW cm⁻².

Characterization.

Solution ^1H NMR experiments were performed on a Bruker DMX 300 NMR spectrometer (300 MHz) with D_6 -dimethyl sulfoxide as the standard. The chemical shift data were later processed by the MestReNova Program. Differential scanning calorimetry (DSC) was performed using a Q2000 DSC (TA Instruments-Waters LLC, USA) system at a heating rate of $10\text{ }^\circ\text{C}\cdot\text{min}^{-1}$.

XRD patterns were collected using a Rigaku D/max-2500 diffractometer. Sample morphologies were characterized using a Hitachi SU8010 field emission scanning electron microscope (FESEM) and JEOL-2100F TEM. AFM was taken on a Bruker Multimode 8 instrument under the AC mode (tapping mode). X-ray photoelectron spectroscopic (XPS) analysis was performed by an ESCALAB MK X-ray photoelectron spectrometer. The spectra were calibrated using the C1s (284.8 eV). We fit peaks by means of XPS-peak-differenating analysis software called "XPSPEAK4.0". FT-IR spectra were recorded on Bruker Tensor 27 IR spectrometer and the sample was prepared by the KBr pellet method. Specific surface areas and pore size distribution were analyzed on Micromeritics ASAP 2020 N_2 adsorption analyzer using the BET (Brunauer-Emmet-Teller) and BJH (Barrett-Joyner-Halenda) methods, respectively. UV-vis diffuse reflectance spectra (DRS) were obtained on a Model c spectrophotometer equipped with an integrating sphere using BaSO_4 as the reflectance standard. The photoluminescence spectra (PL) were recorded with a Perkin Elme LS-55 spectrophotometer excited with a 325 nm wavelength. Time-resolved diffuse reflectance (TDR) spectroscopy were recorded on an Edinburgh Instruments FLS980 spectrometer.

Density functional theory (DFT) calculation.

In this work, the Becke 3-Lee-Yang-Parr (B3LYP) exchange-correlation functional and the mixed basis set of 6-311++G(d,p) and LANL2DZ were used to optimize the geometry of the monomer and complex (Figure S3). The most stable configuration is obtained by comparing the energy of various structures in the calculation process. All calculations were carried out with the Gaussian 09 package.^[S1]

By calculation, ΔE of $\text{FeCl}_3/\text{urea}$ and $\text{FeCl}_3/\text{urea}/\text{melamine}$ is worked out as -203.1 kJ/mol and -250.1 kJ/mol, respectively. It is concluded that the interaction energy of the ternary system is stronger than the binary system, indicating that the addition of melamine is favorable for the entire system. Moreover, it further rationalizes that the ternary system is more dispersed, which contributes to the later sintering process. Moreover, as can be observed, the binding of $\text{FeCl}_3/\text{urea}/\text{melamine}$ is completed by means of hydrogen bond, suggesting the solution is a mixture of hydrogen bond donor (HBD) and hydrogen bond acceptor (HBA). Therefore, we assume that a deep eutectic solvent based on $\text{FeCl}_3/\text{urea}/\text{melamine}$ is formed.

2. Supplementary Figures and Discussion

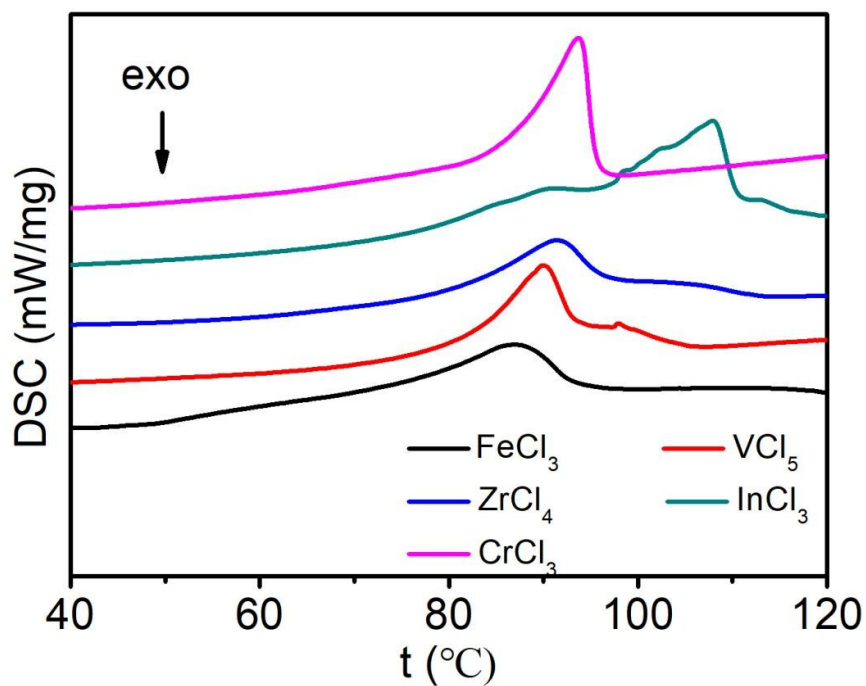


Figure S1. Differential Scanning Calorimeter(DSC) spectra of FeCl₃/urea/melamine, VCl₃/urea/melamine, ZrCl₄/urea/melamine, InCl₃/urea/melamine, and CrCl₃/urea/melamine.

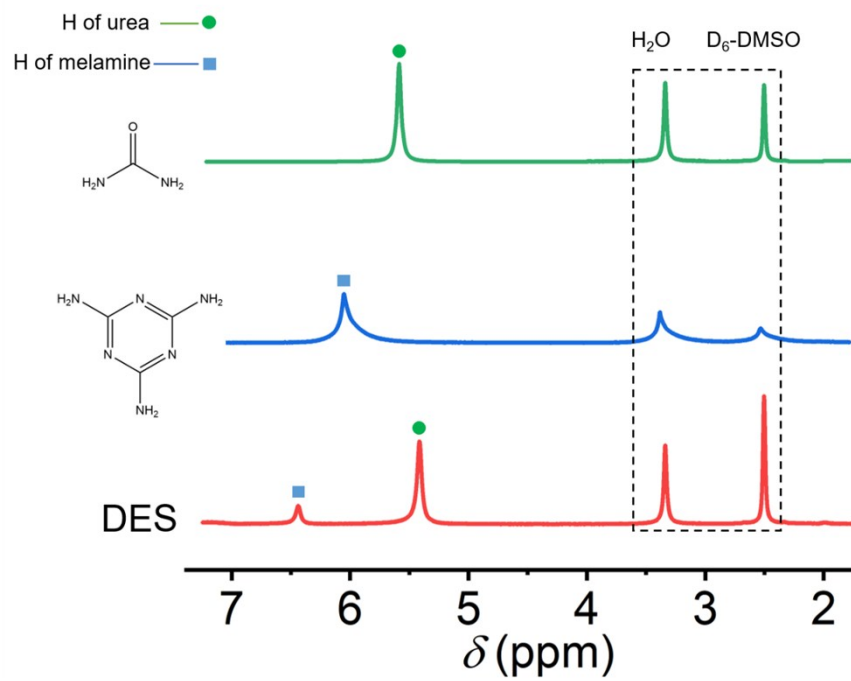


Figure S2. ¹H NMR spectra of urea, melamine and urea/melamine/FeCl₃. The solvent is D₆-DMSO.

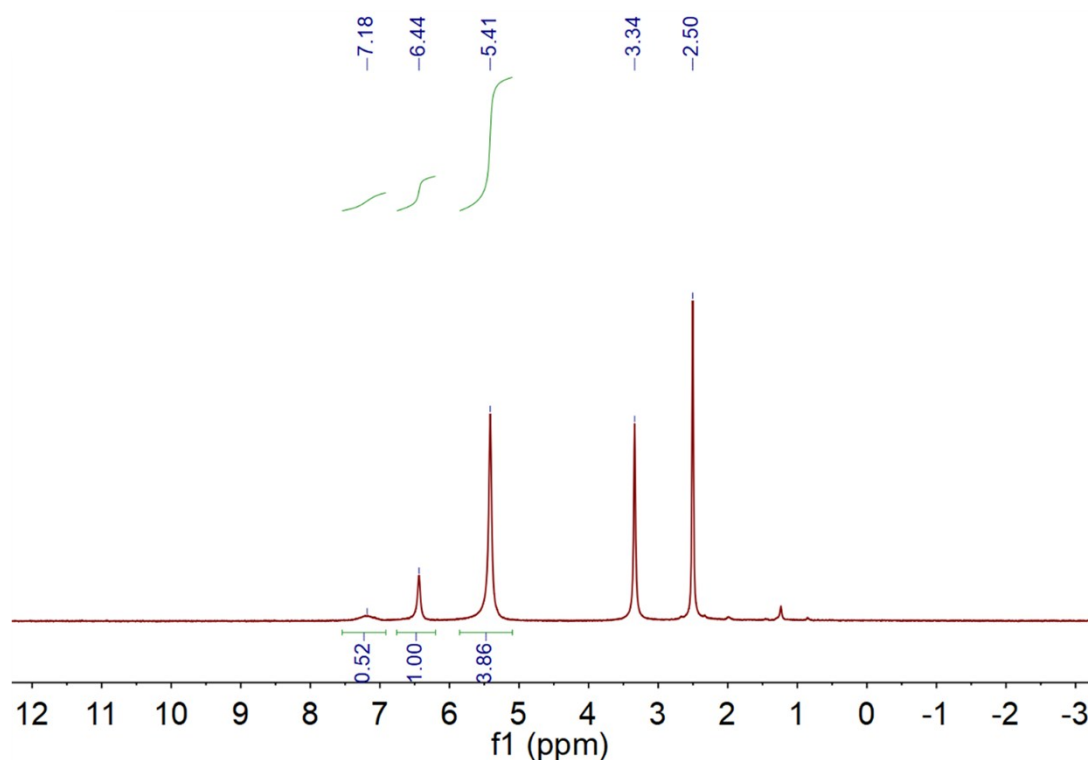


Figure S2b. ^1H NMR spectrum of urea/melamine/ FeCl_3 .

The DES was chosen to carry out nuclear magnetic resonance experiment (Figure S2b).

Since the formed DES is a mixture, we did the following calculations. Combined with the integration of the NMR spectrum, we determined that there is indeed a hydrogen bond in DES.

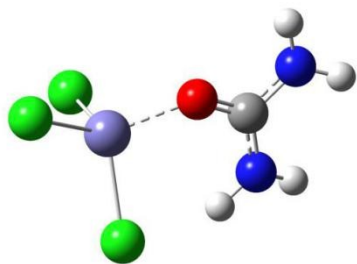
A urea molecule contains 4 hydrogens, so the $H_{(\text{urea})}$ is $0.12 \times 4 = 0.48$ mol.

A melamine molecule contains 6 hydrogens, so the $H_{(\text{melamine})}$ is $0.1092 \times 6 = 0.1092$ mol.

Therefore, $H_{(\text{urea})}:H_{(\text{melamine})} = 0.48:0.1092 = 4.4:1$.

Peak at 6.44 ppm belongs to melamine, it just shifted. However, the characteristic peak of urea not only shifted but split as well. The broad peak appearing at 7.18 ppm corresponds to the formation of a hydrogen bond. Besides, the integrated area ratio of the peaks is $H_{(\text{urea})}:H_{(\text{melamine})} = 4.38:1$, which coincides with the calculation above.

a



b

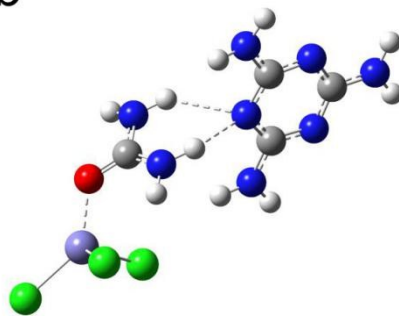


Figure S3. DFT optimized structures of the (a) FeCl₃/urea and (b) FeCl₃/urea/melamine.

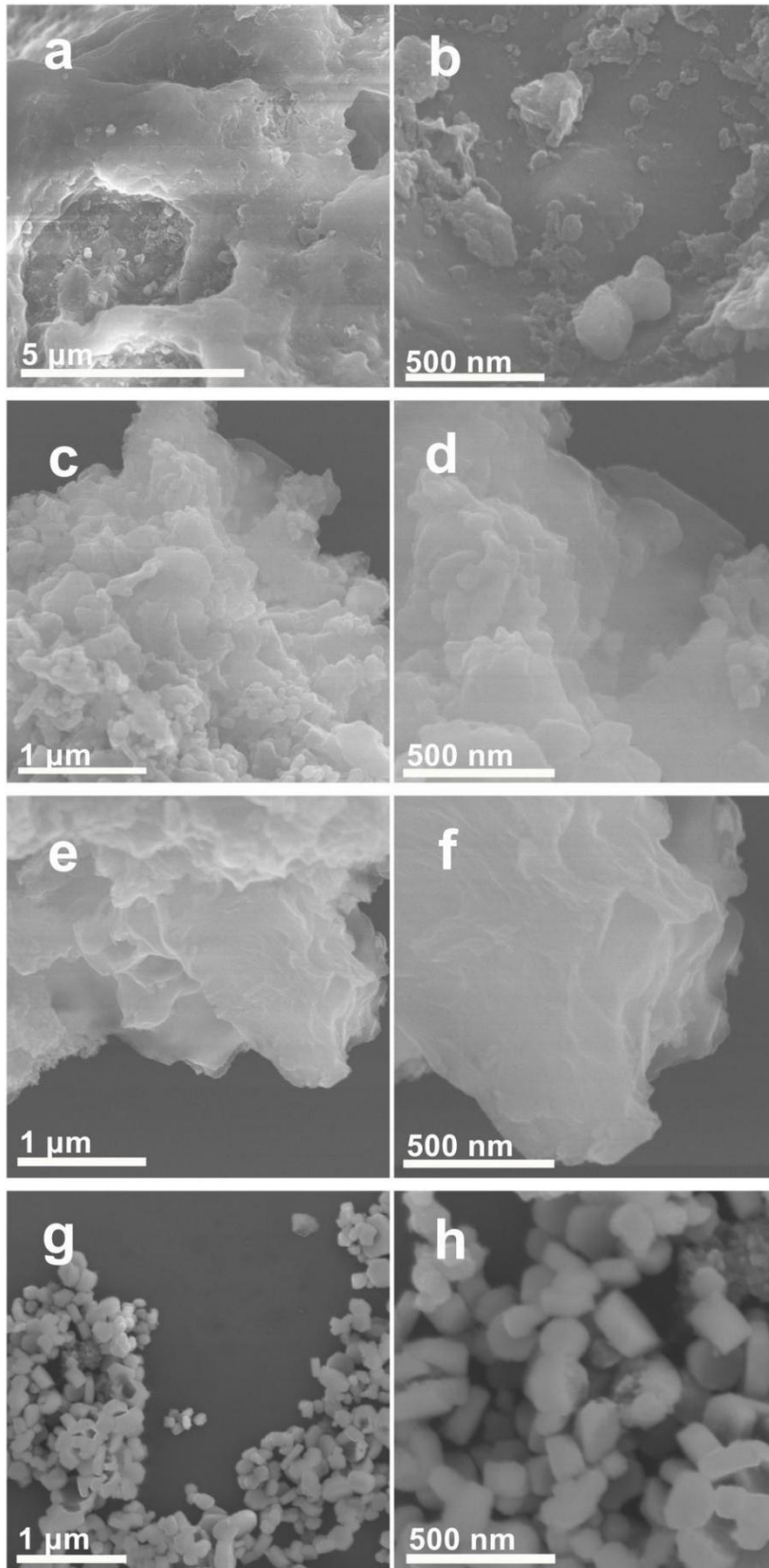


Figure S4. SEM images of a, b) g-C₃N₄/40 wt. % VO₂, c, d) g-C₃N₄/40 wt. % In₂O₃, e, f) g-C₃N₄/40 wt. % ZrO₂, and g, h) g-C₃N₄/40 wt. % Cr₂O₃.

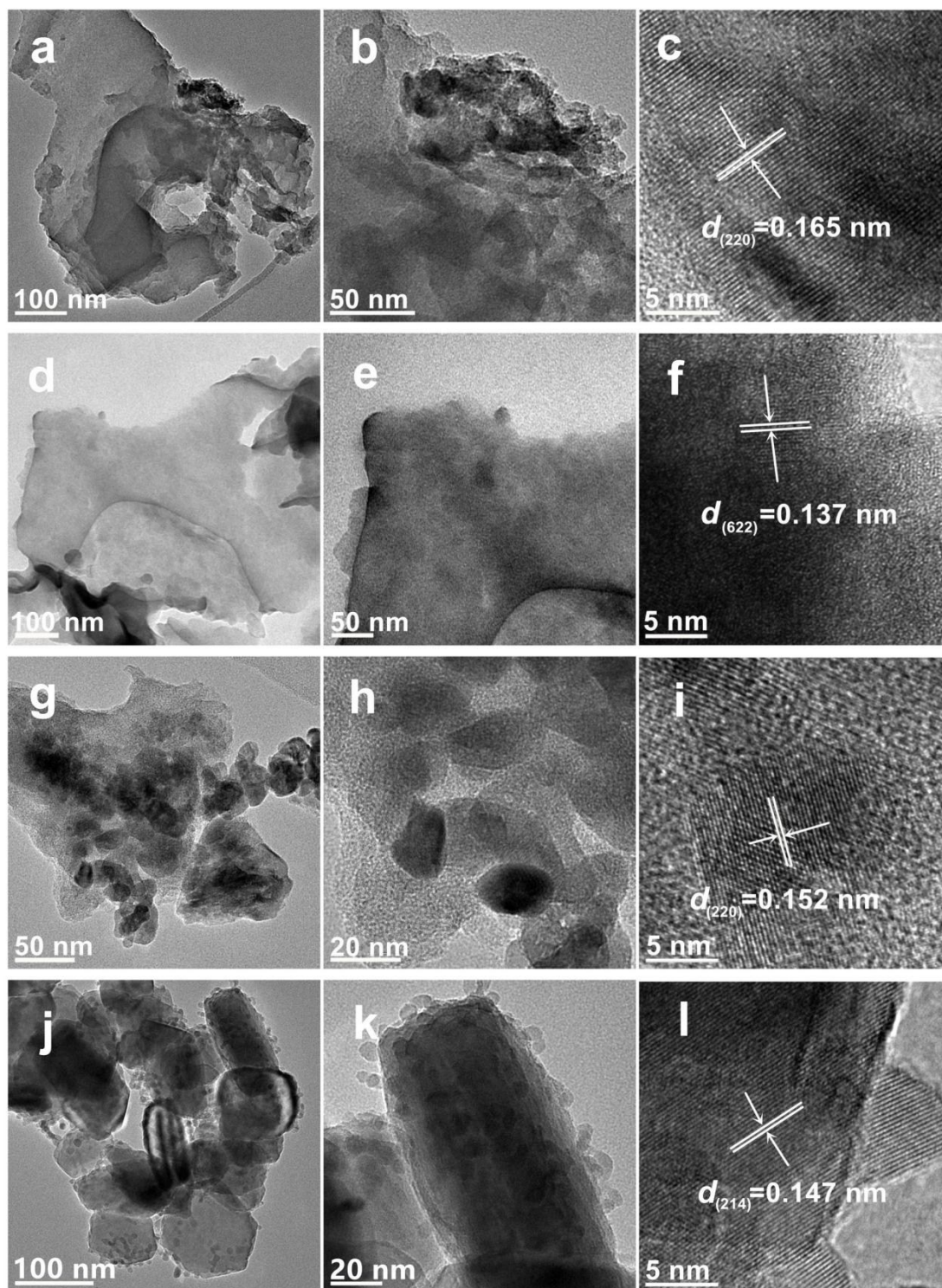


Figure S5. TEM images of a, b) g-C₃N₄/40 wt. % VO₂, d, e) g-C₃N₄/40 wt. % In₂O₃, g, h) g-C₃N₄/40 wt. % ZrO₂, and j, k) g-C₃N₄/40 wt. % Cr₂O₃; HRTEM images of c) g-C₃N₄/40 wt. % VO₂, f) g-C₃N₄/40 wt. % In₂O₃, i) g-C₃N₄/40 wt. % ZrO₂, and l) g-C₃N₄/40 wt. % Cr₂O₃.

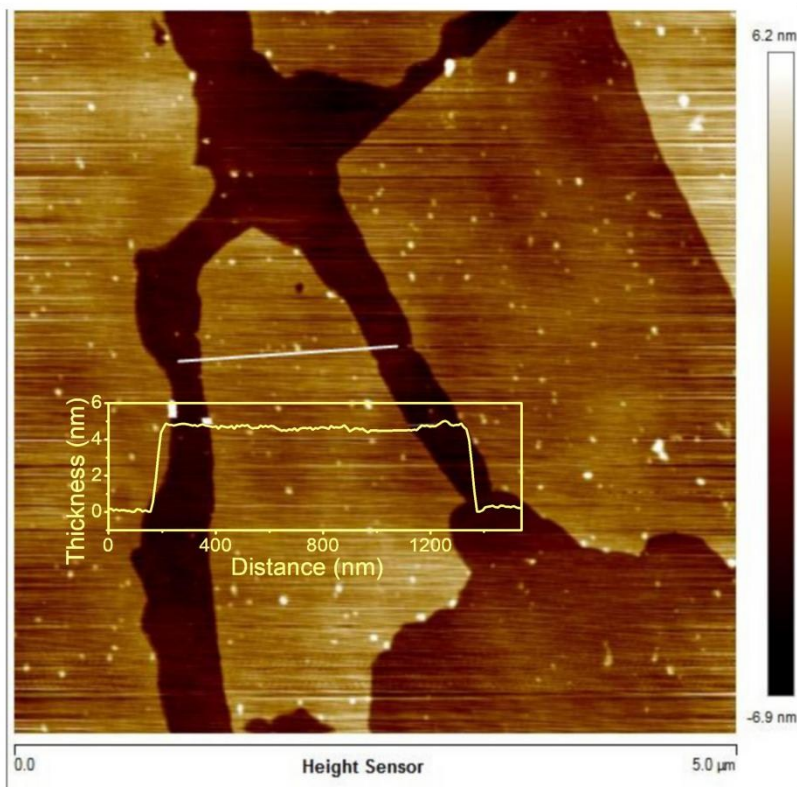


Figure S6. AFM image of the g-C₃N₄/40 wt. % Fe₂O₃.

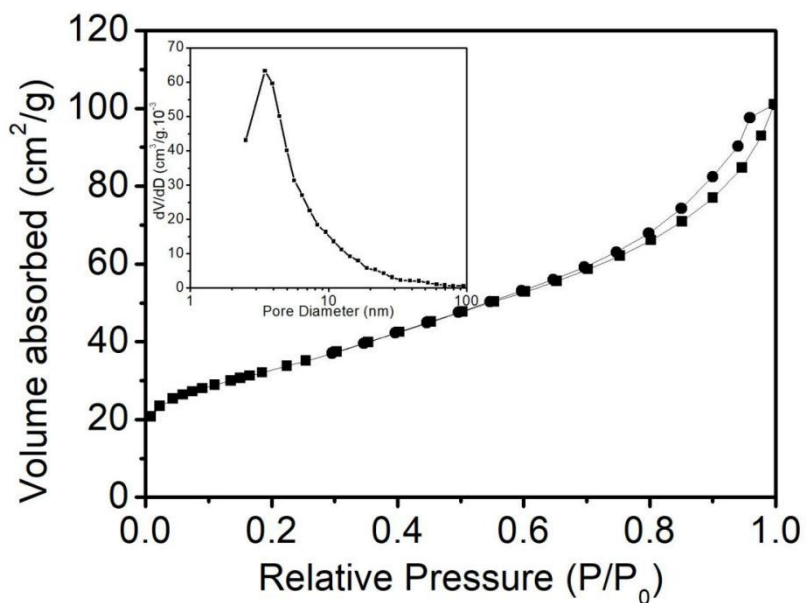


Figure S7. Nitrogen adsorption-desorption isotherm and pore size distribution (inset) of the g-C₃N₄/40 wt. % Fe₂O₃.

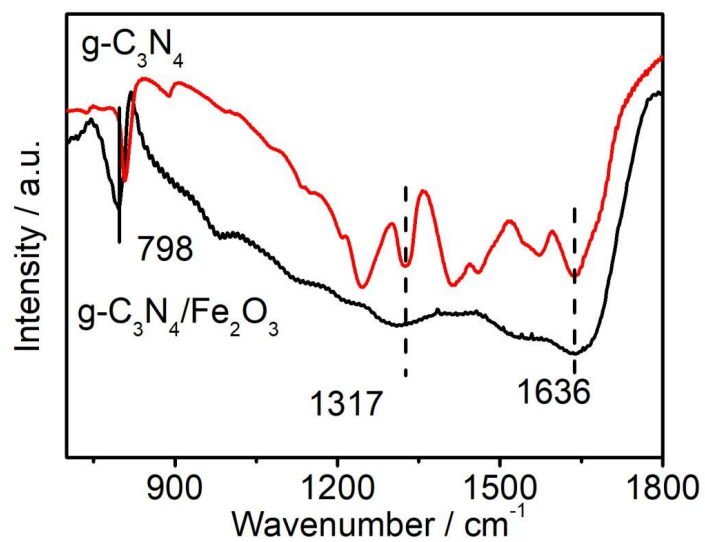


Figure S8. FT-IR spectra of $g\text{-C}_3\text{N}_4$ and $g\text{-C}_3\text{N}_4/40 \text{ wt. } \% \text{Fe}_2\text{O}_3$.

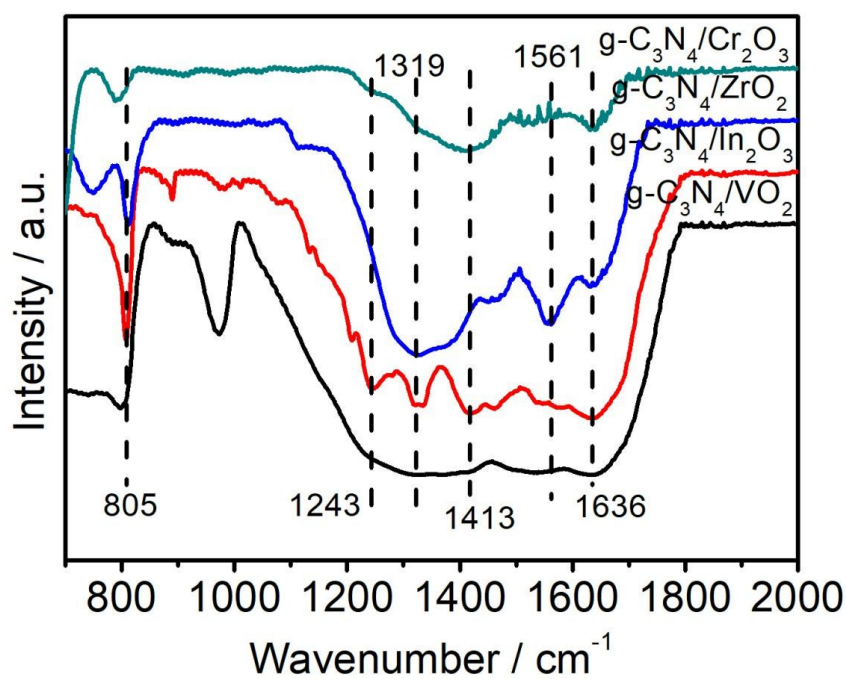


Figure S9. FT-IR spectra of $g\text{-C}_3\text{N}_4/40 \text{ wt. } \% \text{VO}_2$, $g\text{-C}_3\text{N}_4/40 \text{ wt. } \% \text{ZrO}_2$, $g\text{-C}_3\text{N}_4/40 \text{ wt. } \% \text{In}_2\text{O}_3$, and $g\text{-C}_3\text{N}_4/40 \text{ wt. } \% \text{Cr}_2\text{O}_3$.

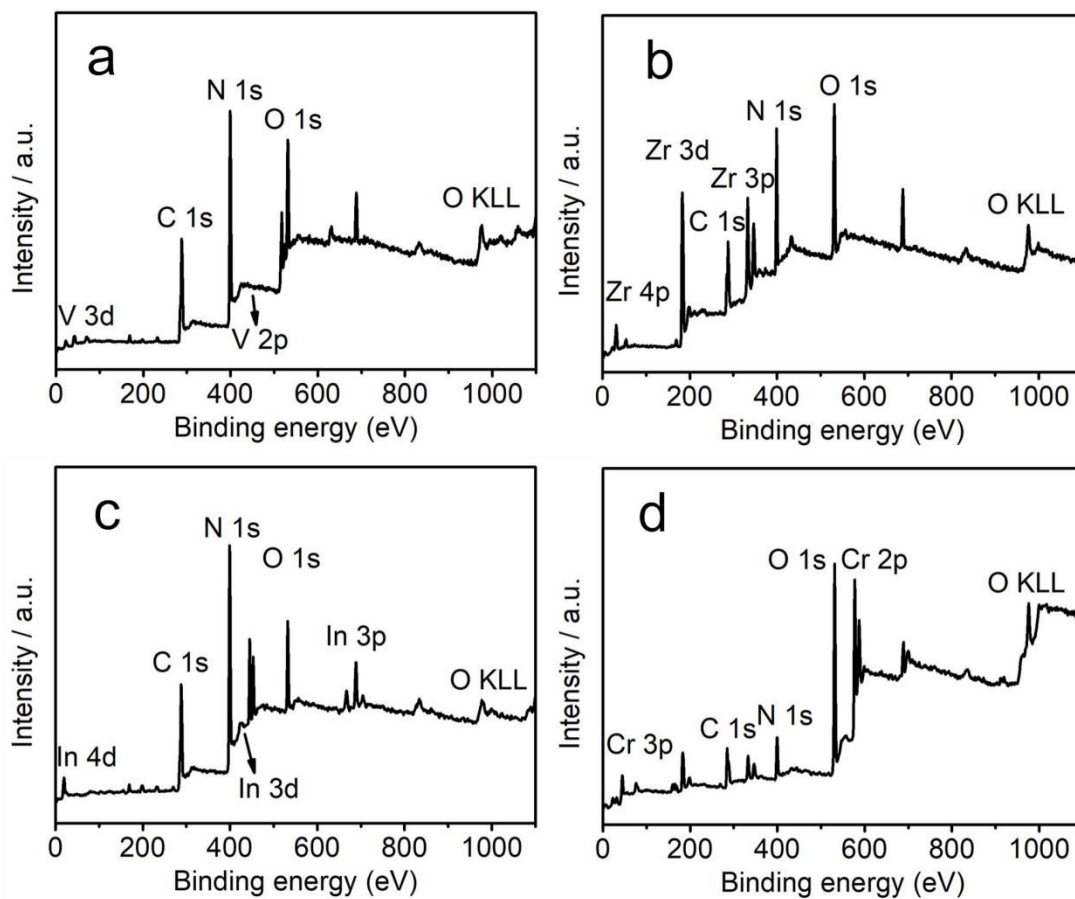


Figure S10. XPS survey spectra of a) $g\text{-C}_3\text{N}_4/40$ wt. % VO_2 , b) $g\text{-C}_3\text{N}_4/40$ wt. % ZrO_2 , c) $g\text{-C}_3\text{N}_4/40$ wt. % In_2O_3 , and d) $g\text{-C}_3\text{N}_4/40$ wt. % Cr_2O_3 .

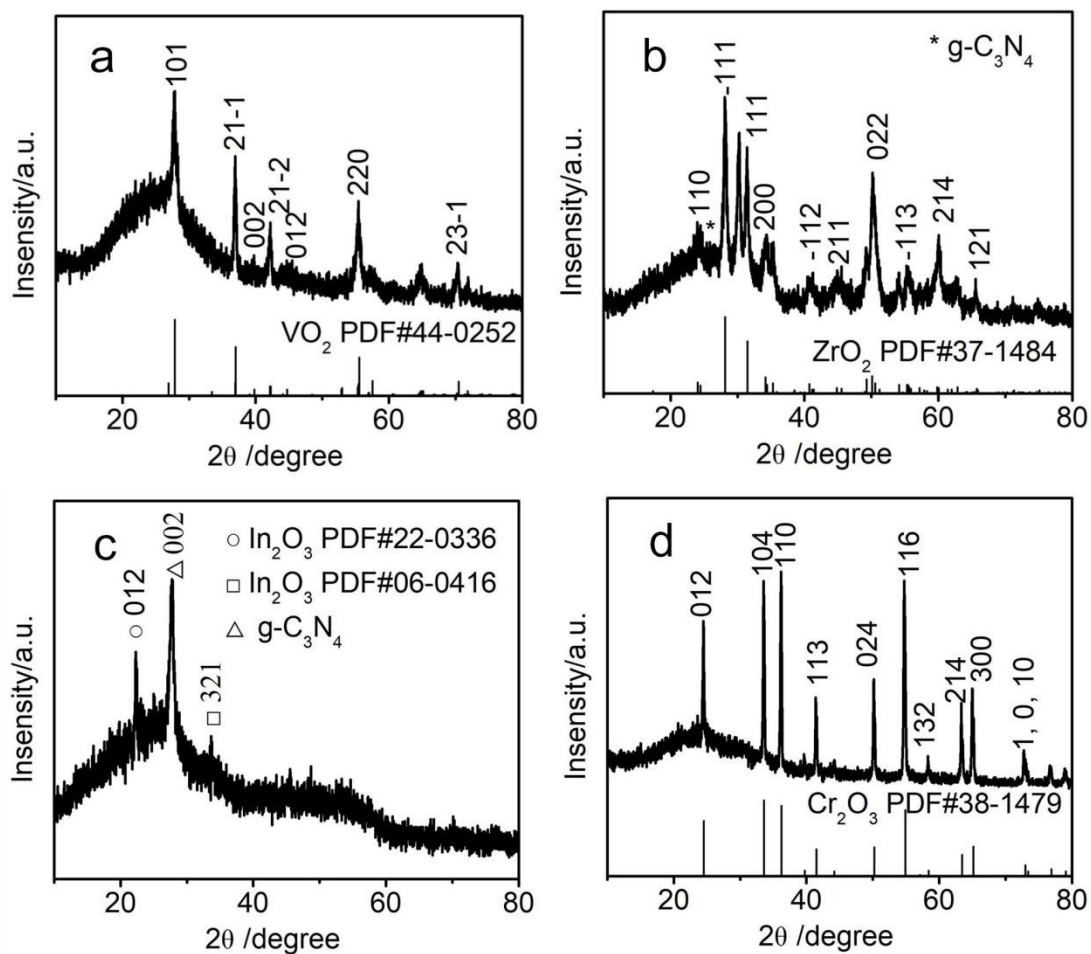


Figure S11. XRD patterns of a) $g-C_3N_4/40$ wt. % VO_2 , b) $g-C_3N_4/40$ wt. % ZrO_2 , c) $g-C_3N_4/40$ wt. % In_2O_3 , and d) $g-C_3N_4/40$ wt. % Cr_2O_3 .

To demonstrate the electron transfer of Fe_2O_3 in the $\text{g-C}_3\text{N}_4/\text{Fe}_2\text{O}_3$ materials, photoelectrochemical measurements with photocurrent responses, current density-potential (J-V), and electrochemical impedance spectroscopy (EIS) of different Fe_2O_3 loading amount were investigated under visible light irradiation and shown in Figure S12. When the $\text{g-C}_3\text{N}_4/\text{Fe}_2\text{O}_3$ modified electrodes (Figure S12a) were illuminated, response photocurrents with repeatable on/off cycles were observed. The responsive photocurrents for $\text{g-C}_3\text{N}_4/\text{Fe}_2\text{O}_3$ (mass ratio varies from 30, 35, 40 to 50 wt. %) are ca. 11.3, 12.6, 44.0, 45.8, and 52.5 $\mu\text{A}\cdot\text{cm}^{-2}$, respectively. And $\text{g-C}_3\text{N}_4/40$ wt. % Fe_2O_3 showed the highest current density (52.5 $\mu\text{A}\cdot\text{cm}^{-2}$). The J-V curves in Figure S12b shows that the current density followed the same trend. It was attributed to the highest efficiency of interfacial charge transfers in moderate load $\text{g-C}_3\text{N}_4/\text{Fe}_2\text{O}_3$ heterostructures. Importantly, when the electrodes were upon light irradiation, the current densities improved greatly compared to current densities under dark condition, in which $\text{g-C}_3\text{N}_4/40$ wt. % Fe_2O_3 showed the highest current density and reached to 5.2 $\text{mA}\cdot\text{cm}^{-2}$. This result suggests $\text{g-C}_3\text{N}_4/\text{Fe}_2\text{O}_3$ absorbed photons and generated electrons under light irradiation. As higher charger separation efficiency resulted in higher photocurrent densities, $\text{g-C}_3\text{N}_4$ with 40 wt. % Fe_2O_3 loading gives the highest charger separation efficiency.

In addition, EIS of above electrodes were measured to verify the internal resistances and interfacial electron transfers of the samples. Usually, the semicircle arc in the EIS spectra is used to evaluate the interfacial electron transfer, and smaller semicircle arc means faster interfacial electron transfer.^[S2] Under light irradiation, the smaller diameter of the semicircle arc for the $\text{g-C}_3\text{N}_4/40$ wt. % Fe_2O_3 heterostructure compared to the diameter of other samples indicated efficient interfacial charge mobility for $\text{g-C}_3\text{N}_4/40$ wt. % Fe_2O_3 . These results suggest an effective interfacial charge transport upon light irradiation, and the heterostructure of $\text{g-C}_3\text{N}_4/40$ wt. % Fe_2O_3 gives the highest efficiency of interfacial charge transport (Figure S12c).

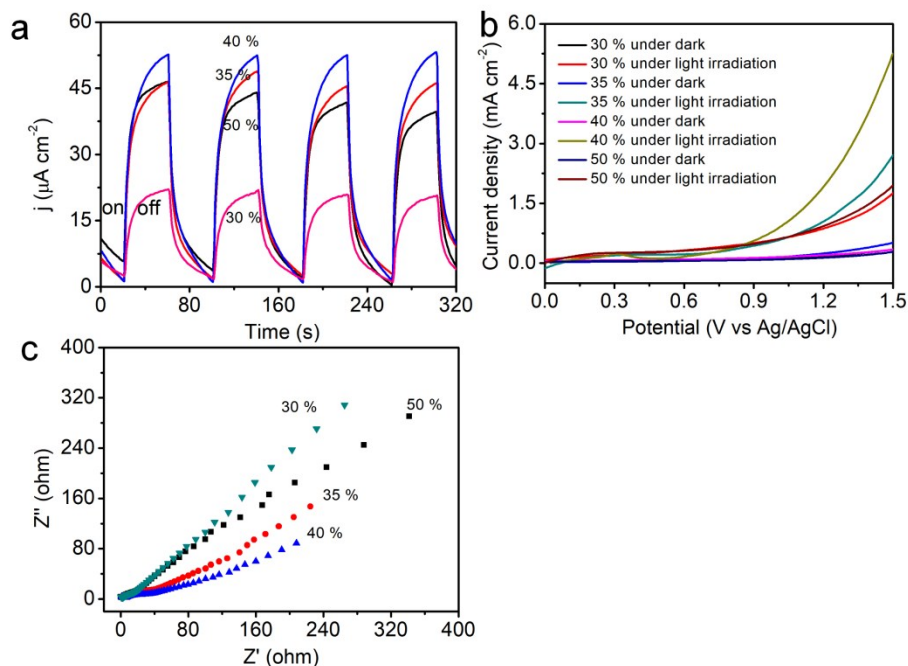


Figure S12. Photocurrent responses of g-C₃N₄/30 wt. % Fe₂O₃, g-C₃N₄/35 wt. % Fe₂O₃, g-C₃N₄/40 wt. % Fe₂O₃, and g-C₃N₄/50 wt. % Fe₂O₃ under light irradiation (a). J-V curves (b) and EIS spectra (c) of different samples in 0.5 M Na₂SO₄ solution under dark and visible light irradiation.

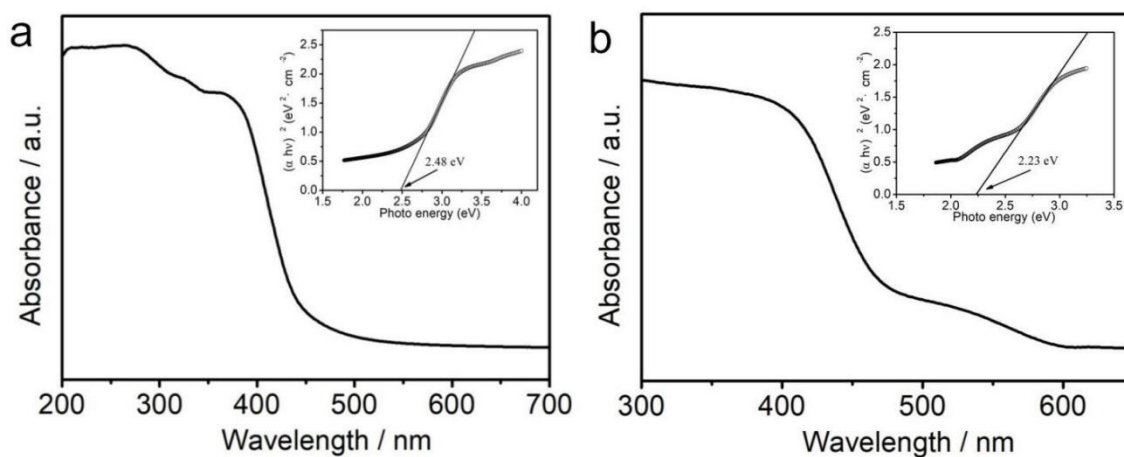


Figure S13. UV-vis DRS of a) g-C₃N₄ and b) α -Fe₂O₃ (insert image: the plot of $(\alpha h\nu)^2$ versus $h\nu$).

The optical properties of g-C₃N₄ and α -Fe₂O₃ were analyzed by UV/Vis diffuse reflectance spectroscopy. As shown in Fig. S13, g-C₃N₄ nanosheets and α -Fe₂O₃ nanoparticles have major absorption at wavelengths smaller than 500 nm and 556 nm, respectively. According to the change of $(\alpha h\nu)^2$ and $h\nu$, the energy band gap of g-C₃N₄ and α -Fe₂O₃ samples was 2.48 eV and 2.23 eV, respectively.

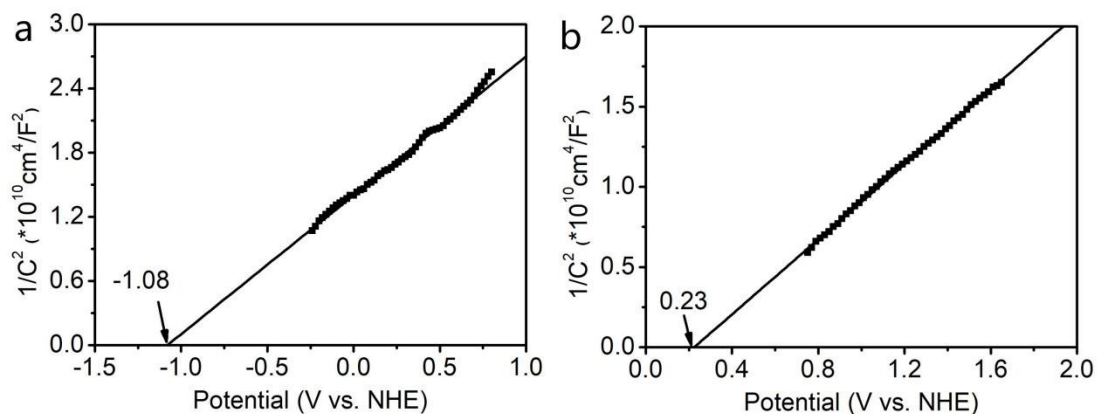


Figure S14. Mott-Schottky plots of a) $g\text{-C}_3\text{N}_4$ and b) $\alpha\text{-Fe}_2\text{O}_3$

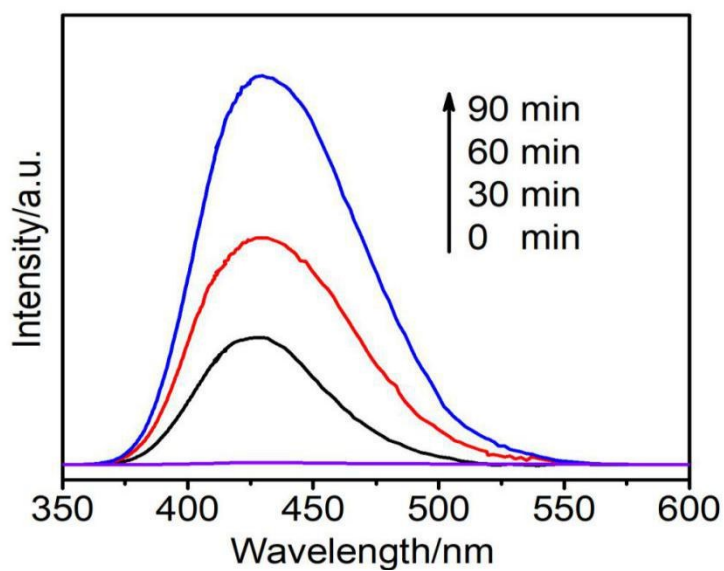


Figure S15. The $g\text{-C}_3\text{N}_4/40 \text{ wt. } \% \text{ Fe}_2\text{O}_3$ of PL intensity@425 nm in 2 mM NaOH solution with presence of 0.5 mM terephthalic acid.

3. Supplementary Tables

Table S1. Elemental analysis results of the g-C₃N₄/Fe₂O₃.

photocatalyst	C wt %	N wt %	H wt %	C/N atom ratio
g-C ₃ N ₄ /30 wt. % Fe ₂ O ₃	26.85	45.05	1.32	0.695
g-C ₃ N ₄ /35 wt. % Fe ₂ O ₃	24.77	42.03	0.91	0.687
g-C ₃ N ₄ /40 wt. % Fe ₂ O ₃	22.83	37.6	1.18	0.708
g-C ₃ N ₄ /50 wt. % Fe ₂ O ₃	19.68	33.12	1.15	0.693

Table S2. Kinetic parameters of transient absorption decays of g-C₃N₄/Fe₂O₃, under 360 nm excitation with time profiles of absorption probed at 505 nm.

photocatalyst	τ_1 (ps)	τ_2 (ps)	average lifetime (ps)
g-C ₃ N ₄ /30 wt. % Fe ₂ O ₃	40(79.13 %)	1040(20.87 %)	248.7
g-C ₃ N ₄ /35 wt. % Fe ₂ O ₃	50(77.68 %)	1070(22.32 %)	278.2
g-C ₃ N ₄ /40 wt. % Fe ₂ O ₃	100(78.60 %)	1100(21.40 %)	314.0
g-C ₃ N ₄ /50 wt. % Fe ₂ O ₃	70(78.23 %)	1060(21.77 %)	285.5

4. References

- [1] M. J. Frisch, G. W. Trucks, H. B. Schlegel, G. E. Scuseria, M. A. Robb, J. R. Cheeseman, G. Scalmani, V. Barone, B. Mennucci, G. A. Petersson, H. Nakatsuji, M. Caricato, X. Li, H. P. Hratchian, A. F. Izmaylov, J. Bloino, G. Zheng, J. L. Sonnenberg, M. Hada, M. Ehara, K. Toyota, R. Fukuda, J. Hasegawa, M. Ishida, T. Nakajima, Y. Honda, O. Kitao, H. Nakai, T. Vreven, J. J. A. Montgomery, J. E. Peralta, F. Ogliaro, M. Bearpark, J. J. Heyd, E. Brothers, K. N. Kudin, V. N. Staroverov, T. Keith, R. Kobayashi, J. Normand, K. Raghavachari, A. Rendell, J. C. Burant, S. S. Iyengar, J. Tomasi, M. Cossi, N. Rega, J. M. Millam, M. Klene, J. E. Knox, J. B. Cross, V. Bakken, C. Adamo, J. Jaramillo, R. Gomperts, R. E. Stratmann, O. Yazyev, A. J. Austin, R. Cammi, C. Pomelli, J. W. Ochterski, R. L. Martin, K. Morokuma, V. G. Zakrzewski, G. A. Voth, P. Salvador, J. J. Dannenberg, S. Dapprich, A. D. Daniels, O. Farkas, J. B. Foresman, J. V. Ortiz, J. Cioslowski and D. J. Fox, Gaussian 09, Revision C.01, Gaussian, Inc., Wallingford, CT, 2010.
- [2] Adachi, M.; Sakamoto, M.; Jiu, J. T.; Ogata, Y.; Isoda, S. *J. Phy. Chem. B* 2006, **110**, 13872-13880.